

Bond-breaking analyses on the characteristics of flow defects in metallic glasses under plastic deformation

Shaopeng Pan^{1,2}, Guang-Ping Zheng^{2,*}, Junwei Qiao¹, Xiaofeng Niu¹,
Weimin Wang³, Jingyu Qin³

¹*College of Materials Science and Engineering, Taiyuan University of Technology,
Taiyuan, 030024, China*

²*Department of Mechanical Engineering, The Hong Kong Polytechnic University,
Hung Hom, Kowloon, Hong Kong, 999077, China*

³*Key Laboratory for Liquid-Solid Structural Evolution and Processing of Materials
(Ministry of Education), Shandong University, Jinan 250061, China*

Abstract

Bond breaking related with plastic deformation in a deformed metallic glass $Zr_{50}Cu_{50}$ is investigated by molecular dynamics simulations. The results show that the spatial distributions of broken bonds are closely correlated with local shear strains, and the clustering behaviors of atoms with broken bonds (flow defects) are characterized with different stages of plastic deformation. The average distance among those clusters of flow defects decreases as the strains increase, which follows the curvature quadrupole model for flow defects in ideal amorphous solids. For the first time, the features of bond breaking processes are quantitatively measured with the chemical composition, bond length and orientation, bond pairs, local five-fold symmetry and quasi-nearest atoms, whose threshold values are important factors that could characterize the flow defects in metallic glasses under plastic deformation. The shape, orientation and energetics of flow defects quantitatively characterized by the bond breaking analysis thus facilitate our understanding on the deformation mechanisms in metallic glasses.

Keywords: Metallic glasses; Structural defects; Bond breaking; Local atomic structure; Molecular dynamics simulations

* To whom the correspondence and request for materials should be addressed.

(Email:mmzheng@polyu.edu.hk).

1. Introduction

Metallic glasses (MGs) have become a kind of new material due to their high mechanical strength, large elastic strain, good corrosion resistance and excellent soft magnetic property [1-6]. However, their room temperature brittleness seriously restricts their application [7]. Although many efforts have been devoted to improving the ductility of MGs, few MGs have been used as structural materials [8]. One of the reasons is that the deformation mechanism in MGs is still unclear, though it has been studied for many years [9-12]. Some theories and models, such as free volumes [13], shear transformation zones [14-15], and flow units [16-17] have been proposed to uncover the deformation mechanism. However, currently, due to the poor descriptions on the atomic structures of MGs [18], the accurate structural features of those proposed models have not been fully established yet. Compared to those in periodically packed crystals, conventional defects such as dislocations and grain boundaries do not exist in MGs [19]. The numbers of the nearest neighbors for most of atoms with the same atomic type in covalently bonded glasses, such as oxide and silicate glasses, usually remain unchanged throughout the glassy structures due to their strong chemical interaction [20]. Therefore, the dangling bond is widely regarded as a structural defect in covalent bonded glasses [20]. These structural

defects play an important role as the carriers of plastic flows in the deformation of those glassy materials. In MGs, on the contrary, the coordination numbers for most of atoms are variable owing to the flexible metallic bonds [21]. Therefore, the dangling bond is difficult to observe in MGs. Although the structural defects in MGs have not been described well, the deformation mechanisms in MGs might be unveiled from other perspectives. In general, the movement of defects in the deformations of solids is achieved by the breakage and recreation of bonds. Therefore, the deformation mechanisms might be well understood from the chemical, structural and dynamical characteristics of bond breaking in MGs under plastic deformations [22]. Based on the position of the first minimum in pair distribution function [23], the critical bond length could be found to define the existence and the breakage of metallic bonds. Consequently, the concept of bond breakage and recreation has been used to explain the flow in simple metallic liquids under shear [24] and the anisotropy in MGs under stress [25-26]. Nonetheless, an in-depth understanding on the chemical and structural factors that determine the behaviors of bond breaking in MGs, and the relationship between the plasticity and bond breaking processes has not been established.

Because there is a lack of long-range periodic structures, MGs are extremely complex in atomic structures. Compared with the dislocation in conventional alloys which can be well characterized by a slip system with quantitative measures of Burgers vectors and slip planes, the microscopic structural defects in MGs are rather qualitatively described by the local strain entities such as the free-volume defects [13] and shear-transformation zones [14-15]. Therefore, the mechanistic understanding of plasticity in MGs is a grand challenge, particularly in the atomic scales. For instance, what geometry, orientation and energetics of the microscopic structural defects should be and how they response to the thermo-mechanical excitation, which determine the

relationships between the atomic structures and mechanical properties of MGs, yet remain unknown. The information on bond breaking thus provides valuable insights for us to develop a new microscopic model of structural defects and to address the atomic structure-mechanical property relationship in MGs.

In this paper we systematically characterize the bond breaking processes in a model MG $Zr_{50}Cu_{50}$ under uniaxial compression through molecular dynamics (MD) simulations. The flow defects are identified by the bond-breaking analysis, and their mechanistic behaviors correlated with plasticity in MGs are thus established. Moreover, the chemical and structural factors that affect the behaviors of bond breaking are quantitatively measured. The geometry, orientation and energetics of flow defects in MGs under plastic deformation can be revealed by the bond breaking analysis.

2. Simulation methods

The bond breaking processes in a model MG $Zr_{50}Cu_{50}$ under uniaxial compression were investigated by MD simulations. Periodic boundary conditions (PBCs) were applied to the system containing 250,000 atoms with an embedded-atom method (EAM) inter-atomic potential [27]. Firstly, the system was melted for 1ns at $T=2000$ K, and quenched to $T=50$ K at a cooling rate of 10^{11} K/s. The system was then relaxed at 50 K for 1 ns. During the sample preparation, constant number, pressure and temperature (NPT) ensemble was applied to the system at zero pressure. After that, we applied compressive deformation on the MG sample along the X -axis with a strain rate of 1×10^{-7} fs $^{-1}$ at $T=50$ K. During the compression, PBCs on three dimensions was set and the pressures along the Y and Z directions were kept at zero.

In metallic liquids and glasses, a bond is usually defined to be located between two nearest-neighbor atoms, which are often determined by the first minimum of pair

distribution function (PDF). Figure 1 shows the partial PDFs for Zr-Zr, Zr-Cu and Cu-Cu pairs in the $Zr_{50}Cu_{50}$ MG sample, whose atomic configuration is also displayed. It can be seen that the first peak of Zr-Cu PDF is much stronger than those of Zr-Zr and Cu-Cu PDFs, indicating that the bonds with different atomic types are more prevalent than those with the same atomic types. The first minimums of PDFs for Zr-Zr (4.17 Å), Zr-Cu (3.69 Å) and Cu-Cu (3.23 Å) are chosen to be the threshold distances for the formation of bonds, i.e., a bond exists between two atoms with a distance less than the corresponding threshold distance. Under a certain applied strain, if the distance between two atoms connected by a bond before uniaxial compression is larger than the corresponding threshold distance, the bond is considered to be broken.

3. Characterization on bond breaking in the deformed MGs

Figure 2 shows the stress(σ)-strain(δ) curve for the model MG under uniaxial compression at 50 K. The stress increases linearly with the strain below 1.9%, which is identified as the elastic limit. After that, the stress begins to deviate from its linear response to the applied strain and continues to increase until about 5.9% strain, beyond which the resulting stress decreases abruptly. At a strain of approximately 9%, the stress starts to decrease slowly, suggesting that the plastic flow occurs in the model MG. In this work, we mainly analyze the flow defects in the sample with an overall strain between 1.9% and 9%.

3.1 The correlation between bond breaking and local shear strains

To measure the rearrangements of atomic structure of samples under compressive deformation, local shear strain, η_i^{Mises} [28], is calculated for a configuration at a certain strain with the reference of the initial one. Similar to the non-affine displacement (D_{min}^2) defined by Falk and Langer [29], η_i^{Mises} can well characterize the local inelastic deformation in MGs. In this work, η_i^{Mises} is calculated

by OVITO software [30].

Bond breaking can be considered as the conformation of large atomic rearrangement, whereas there must be some correlations between the bond breaking and local shear strains. We first analyze the number of broken bonds (n_B) for each atom at some strains. Figure 3 shows the statistical distribution of η_i^{Mises} for the atoms with different n_B and that for the total atoms, at 2%, 4%, 6% and 8% strains. For all the stains, the highest peaks are all owned by the atoms with $n_B=0$ and centered at a small average η_i^{Mises} ($\langle \eta_i^{Mises} \rangle$), which indicates that most of the atoms with $n_B=0$ could correspond to small atomic rearrangements. As n_B increases, the peak becomes a little weaker, and shifts toward larger $\langle \eta_i^{Mises} \rangle$. The insets in Fig. 3 show that the $\langle \eta_i^{Mises} \rangle$ increases with increasing n_B , suggesting a strong correlation between n_B and η_i^{Mises} under plastic deformation.

Figure 4 displays the spatial distributions of n_B and η_i^{Mises} in the early stage of plastic deformation at an overall strain of 6%, with the atoms colored by η_i^{Mises} and n_B . It is noted that the regions with large η_i^{Mises} and those with high n_B are almost overlapped while most of the atoms with small η_i^{Mises} are located in the region with low n_B , unambiguously reflecting the close spatial correlation between the bond breaking and atomic rearrangement under plastic deformation in MGs. We check the spatial distributions of n_B and η_i^{Mises} at a higher strain 15% and found that the correlation seems much better than that at 6%.

In order to quantitatively characterize the correlation between n_B and η_i^{Mises} , we calculate their Pearson correlation coefficient $C_p(n_B, \eta_i^{Mises})$ as follows:

$$C_p(n_B, \eta_i^{Mises}) = \frac{E\{[n_B - E(n_B)][\eta_i^{Mises} - E(\eta_i^{Mises})]\}}{D(n_B)D(\eta_i^{Mises})}, \quad (1)$$

where $E(x)$ and $D(x)$ measure the average values and the standard deviations of x ,

respectively. $C=1$ or $C=-1$ represents maximum correlation while $C=0$ means no correlation. The Pearson correlation coefficient is usually used to describe the linear correlation. Meanwhile, we also calculate the Spearman's rank correlation coefficient as follows:

$$C_s(n_B, \eta_i^{Mises}) = 1 - \frac{6 \sum d_i^2}{N(N^2-1)}, \quad (2)$$

where d_i is the difference between the two ranks of n_B and η_i^{Mises} for atom i . N is the total number of atoms in the systems. Figure 5 shows $C_p(n_B, \eta_i^{Mises})$ and $C_s(n_B, \eta_i^{Mises})$ at different overall strains. At the strain of 1%, $C_p(n_B, \eta_i^{Mises})$ is about 0.1, indicating a small linear correlation between the bond breaking and atomic arrangement. However, $C_s(n_B, \eta_i^{Mises})$ is about 0.35, suggesting a much larger monotonous correlation. As the strain increases, the value of $C_p(n_B, \eta_i^{Mises})$ linearly increases with the strain lower than about 6%. The difference between $C_p(n_B, \eta_i^{Mises})$ and $C_s(n_B, \eta_i^{Mises})$ becomes rather small at 6% strain, which is maintained to be small until about 9% strain. The consistence of $C_p(n_B, \eta_i^{Mises})$ and $C_s(n_B, \eta_i^{Mises})$ between 6% and 9% strains indicates that the correlation between n_B and η_i^{Mises} could be linear at the strain range. When the strain is larger than about 9%, both correlation coefficients become saturated, suggesting either the growth of n_B or η_i^{Mises} could reach a steady state. The results thus suggest a strong correlation between bond breaking and atomic arrangement, demonstrating that the bond breaking plays a key role in MGs under plastic deformation.

3.2 The evolution of bond breaking

Since the bond breaking and atomic arrangement in MGs under plastic deformation are closely correlated, we thereby investigate the detailed evolution of bond breaking as the overall strain increases. The strain dependence of the fraction of

broken bonds is shown in Fig. 6(a). As the strain increases, the fraction of broken bonds increases as expected. However, the growing rate is different at different stages of plastic deformation. The growing rate of the broken bonds increases with increasing strain below 9%, while it keeps almost unchanged when the deformed MG comes to the stage of steady plastic flow, i.e., with a strain larger than 9%. We also investigate the fractions of atoms with different numbers of broken bonds, as shown in Fig. 6(b). At the early stage of uniaxial compression, most of the atoms in the system have no broken bond. The atoms that experience with one or more broken bonds could increase with increasing strains.

As pointed out by the theory of shear transformation zone (STZ) [14], there are at least several dozens or even hundreds of atoms involved in the occurrence of plastic flow in MGs. In comparison with the STZ defects, we define the flow defects in MGs as clusters that are formed by those atoms with broken bonds. Cluster analysis on the atoms with at least one broken bond is performed to identify them as flow defects. Figure 7(a) shows the strain dependence of the number of clusters of flow defects, N_c . As strain increases, N_c first increases, and reaches the maximum and then decreases. There might be two effects on the change of N_c . One is the change in the number of atoms with the broken bonds, which results in the increase of N_c with increasing strains. The other is the coalescence of clusters of flow defects, which makes N_c decrease. At the early stage of uniaxial compression, the first effect is predominant. Thus, N_c increases with increasing strains. As the strain increases, there are more events of coalescence of clusters of flow defects, which could much reduce N_c and offset the first effect. Therefore, N_c reaches the maximum at about 6% strain, at which the ultimate stress occurs. When the second effect becomes dominant, N_c begins to decrease, indicating massive coalescence of clusters of flow defects. Figure 7(b)

displays the mean size of clusters, $\langle S_c \rangle$, as a function of strain, where S_c is defined as the number of atoms with broken bonds in the cluster. At the early stage of uniaxial compression, $\langle S_c \rangle$ keeps almost unchanged. After the ultimate stress occurs at a strain of 6%, $\langle S_c \rangle$ begins to grow, in consistent with the change of N_c . The size of the largest cluster, S_{max} , as a function of strain is shown in Figure 7(c). Similar to $\langle S_c \rangle$, S_{max} changes a little at a strain lower than 6%, and it increases rapidly with increasing strain after the ultimate stress occurs.

Besides the sizes of clusters of flow defects, we also investigate the projected lengths of the largest cluster along x-, y- and z-directions normalized by the system sizes along the three directions, respectively. As shown in Figure 7(d), at a strain below 4%, the normalized projected lengths (NPLs) of the largest cluster along the y-direction is apparently larger than those along other directions, suggesting the ramification of the cluster of flow defects along the longitudinal direction perpendicular to the loading direction at the early stage of plastic deformation. With increasing strains (>4%), NPLs increase and are almost the same along the three directions. They reach about 0.2 when the ultimate stress occurs, and 1.0 at a strain of 9%. The results thus indicate that the largest cluster of flow defects could percolate along three dimensions when the plastic flow begins to occur in MGs. The aforementioned analyses suggest that the cluster of atoms with broken bonds is closely correlated with the different stages of plastic deformation, and could be quantitatively characterized to represent the flow defects in MGs.

Figure 8 shows the clusters of flow defects with a size no less than 10 atoms at different overall strains. The number of large flow defects can be found to increase and the distance among those clusters of flow defects becomes reduced as the strain increases. Figure 9(a) displays the average distance between the centre of gravity of

one cluster to that of its nearest neighboring cluster ($\langle d_{\min} \rangle$). At the beginning of plastic deformation, $\langle d_{\min} \rangle$ decreases quickly with increasing strains while the downward trend of $\langle d_{\min} \rangle$ becomes slower at the strains larger than 4%. It is meaningful to correlate $\langle d_{\min} \rangle$ with the energetics of flow defects at the early stage of plastic deformation, c.f., at 2-4% strains, since the coalescence of clusters of flow defects does not occur at a strain lower than 4%, as illustrated in Fig. 8(c). In this consideration, Fig. 9(b) shows the log-log plot of the correlation between $\langle d_{\min} \rangle$ and $\sigma - \sigma_y$, where σ_y is the yield stress at 1.9% strain. The dash line in Fig. 9(b) thus indicates a power-law relation at the strains of 2-4% $\langle d_{\min} \rangle \sim (\sigma - \sigma_y)^{-\beta}$, where $\beta=0.45$.

4. The chemical and structural factors that influence the bond breaking

A parameter B_{ij} that measures the preference of bond breaking is defined as follows:

$$B_{ij} = p(i,j)/p_0(i,j) - 1, \quad (3)$$

$$p(i,j) = N_b(i,j)/N_b, \quad (4)$$

$$p_0(i,j) = N(i,j)/N, \quad (5)$$

where $i-j$ refers to the properties of the atoms at the ends of a bond. If only i is used, it refers to the property of a bond. $N_b(i,j)$ is the number of broken $i-j$ bonds and N_b is the total number of broken bonds at a certain overall strain. $N(i,j)$ is the number of $i-j$ bonds and N is the total number of bonds. Therefore, the positive and negative values of B_{ij} indicate a preference and an avoiding of $i-j$ bonds being broken, respectively.

4.1 The effects of chemical elements

The interaction among chemical elements plays an important role in glass forming ability, structure relaxation and other properties in MGs [31-33]. The atomic types of the two atoms connected by a bond must influence the property of the bond. Figure 10 shows the preference of bond breaking B_{ij} with different atomic types as a function of

overall strain. At the beginning of uniaxial compression, B_{ij} for Zr-Cu is negative, indicating that the Zr-Cu bonding is hard to break. The strong interaction between Zr and Cu might be the reason. The values of B_{ij} for the same atomic types are both positive before the ultimate stress occurs. However, B_{ij} for Cu-Cu is much larger than that for Zr-Zr, suggesting that the Cu-Cu bonding is easier to break than Zr-Zr. After the the ultimate stress occurs, B_{ij} for Cu-Cu keeps positive while B_{ij} for Zr-Zr changes from positive to negative, which further confirms the weakness of Cu-Cu bonding.

4.2 The effects of bond length

The bond length could be an important factor that affects the bond breaking. In general, a longer bond is much easier to break. Figure 11 (a)-(c) shows the statistical distributions of the lengths of the broken bonds for Zr-Zr, Zr-Cu and Cu-Cu, respectively. The distributions of all the bonds before uniaxial compression are also displayed in the short dash lines. At the strain of 4%, the peak of the distribution for the broken bonds is located at a rather long bond length, which is close to the threshold distances for the bonding. As the strain increases, the peak shifts to the smaller bond length. The results demonstrate that the bond breaking under uniaxial compression could start from those bonds with longer length, as expected.

Besides the length of bonds, the projected lengths of the broken bonds along the loading (x-) direction L_x could be closely related with bond breaking. The statistical distributions of L_x normalized by the maximum bond length L_{cutoff} at different overall strains, $P(L_x/L_{cutoff})$, are shown in Fig. 11 (d)-(f). It is found that the distributions are independent of the overall strains. If $P(L_x/L_{cutoff})$ is larger than that of the projected length of all the bonds before uniaxial compression (the short dash lines in Fig. 11), those bonds with L_x have a preference to break. For all the Zr-Zr, Zr-Cu and Cu-Cu types of bonds, when L_x/L_{cutoff} is less than about 0.4, the probability $P(L_x/L_{cutoff})$ is

larger than that of all the bonds before uniaxial compression, indicating that those bonds with $L_x < 0.4L_{cutoff}$ tends to break under uniaxial compression. The results suggest that the projected length along the loading direction might play a more important role than the bond length in bond breaking.

4.3 The effects of bond orientation

The more important role of normalized projected length than the bond length itself in bond breaking indicates that the bond orientation might also affect the bond breaking. Figure 12 shows the statistical distribution of the angles θ between the initial orientation of the broken bonds at different overall strains and the loading direction. The distribution of angle between the orientation of all the bonds and the loading direction before the uniaxial compression is also shown in the short dash line. It is found that, at all the strains, for $\theta < 57^\circ$, the probability of the angle is all smaller than that for all the bonds, suggesting that the bonds with an angle less than 57° are difficult to break. For those bonds with $\theta > 57^\circ$, they tend to be broken. It is worth noting that the critical angle $\theta = 57^\circ$ is consistent with the position of the first peak of angle distribution function in MGs [34]. Moreover, the fracture angle observed from experiments is near 57° for some MGs [35]. All these facts indicate that 57° might be an important angle which characterizes the orientation feature of atomic structure of flow defects in MGs.

4.4 The effects of bond pairs

Bond pairs with an index of $ijkl$ was a useful tool to describe the atomic structure in metallic liquids or glasses [36]. In the index, i is usually set to be 1, indicating the existence of a bond between a pair of atoms; j is the number of common nearest neighbors shared by the two given atoms; and k is the number of bonds among the i nearest neighbors. The final number l is usually 1 and if the first three numbers are the

same but the distributions of the bonds are different, l will be set to 2. According to the geometrical features of bond pairs, we classify them into two categories: if the shared neighbors can form a ring, *i.e.* $k = j$, we call them “saturated bond pairs”; otherwise, they are designated as “unsaturated bond pairs” [37]. Figure 13 shows the statistical distribution of main bond pairs in $Zr_{50}Cu_{50}$ MG. The bond pair of 1551 has the largest fraction, indicating that the local five-fold symmetry is dominant in the atomic structure of the model MG. The inset of Figure 13 shows the preference of bond breaking of different bond pairs B_{ij} . All the bond pairs can be classified into two groups. One contains the bond pairs of 1441,1431 and those in minority (named as “others” in the figure), which have a positive value of B_{ij} , indicating that those bonds tend to be broken. The other group includes the bond pairs of 1551, 1421,1422,1541 and 1661. These bond pairs have a negative value of B_{ij} , indicating that those bonds tend to avoid being broken. It should be noted that, when the bond pairs have the same index j , the saturated bond pairs are much easier to be broken than the unsaturated bond pairs. For example, the value of B_{ij} for the saturated bond pair of 1441 is larger than that for the unsaturated bond pair of 1431. Moreover, the value of B_{ij} for 1441 and 1431 is positive while that for 1422 and 1421 is negative, suggesting that the former two are much easier to be broken.

4.5 The effects of local atomic cluster packing of Voronoi polyhedron

Voronoi polyhedron(VP) is one of the most popular methods to characterize the atomic structure of MGs [38]. The VP index is expressed as $\langle n_3, n_4, n_5, n_6 \rangle$, where n_i is the number of faces with i edges in the VP and also represents i -fold symmetry structures. Specially, Peng *et al.* proposed a structural parameter to characterize the degree of local five-fold symmetry as $d_5 = n_5 / \sum n_i$ and found that there is a close correlation between d_5 and plastic deformation in MGs [39]. It is thus speculated that

there might also be some correlations between d_5 and bond breaking in plastic deformation. Figure 14 (a) shows the top 20 VPs in the $Zr_{50}Cu_{50}$ MG sample. These VPs are labeled according to their d_5 and the numbers after the bars are their order numbers. It can be seen that the VP with an icosahedral short-range order labelled by a Voronoi index of $\langle 0,0,12,0 \rangle$ has the third largest population in the sample. The top 2 VPs, $\langle 0,2,8,1 \rangle$ and $\langle 0,2,8,2 \rangle$, have the distorted icosahedral short-range order. To unveil the correlation between VPs and the bond breaking, we display the color maps of B_{ij} with the top 20 VPs at the strains of 2%, 4%, 6% and 8%, as shown in Fig. 14(b)~(e). It can be seen that most of B_{ij} ($i, j \leq 15$) have a negative value, suggesting that the bond with those atomic structure tends to avoid being broken under uniaxial compression. Remarkably, it is found that the values of d_5 for those VPs are all no less than 0.5. Thus, 0.5 might be a threshold of d_5 that can be used to identify those VPs prone to bond breaking under the uniaxial compression. The results thus reflect the close correlation between the five-fold symmetry of local atomic cluster packing and the bond breaking, which is also consistent with Peng's work [39].

4.6 The effects of quasi-nearest atoms

Quasi-nearest atom (QNA) was recently proposed as a new structural parameter to characterize the structural defects in metallic liquids and glasses [40-42]. As pointed out in our previous work [41], more QNAs usually correspond to more structural defects in MGs. Figure 15(a) shows the distribution of the number of QNAs (N_Q) in the MG sample, indicating that the statistical distributions of N_Q around Cu and Zr are similar. The fraction of atoms with more than one QNA is more than 70%, indicating a large number of structural defects in the MG samples. Figure 15 (b)~(c) shows the preference of bond breaking with different N_Q . The values of B_{ij} for the pairs of ($i=0, j=0, 1, 2$), i.e., the bond with a QNA number pair of (0,0), (0,1), or (0,2),

are always negative during the whole uniaxial compression processes. Other B_{ij} , especially for larger N_Q , are almost positive. The results illustrate that the bond with the atoms that possess less QNAs tends to avoid being broken, which is consistent with our previous work [41].

5. The model for flow defects based on the characteristics of bond breaking.

As described in Sec.4.4, the bond breakage preference B_{ij} indicates that those minority bonds (labeled as ‘others’) and bonds in *bcc*-like (1441 type) and defective-*fcc* (1431 type) clusters are prone to breakage in forming flow defects. The results imply that the flow defects could be generated in those clusters that are of geometric incompatibility with the dominant (1551)-icosahedral clusters. Such speculation on the structural properties of flow defects is also demonstrated by the effects of VPs on the bond breaking. As shown in Fig. 14, the bond breaking can be found to occur mostly in those VPs whose local atomic packing is deviated from the five-fold symmetry, with a measure $d_5 < 0.5$. Judging the fact that the local atomic cluster packing in the structural motif is dominated by those VPs (icosahedra or distorted icosahedra) with high local degree of five-fold symmetry ($d_5 \sim 1$), the flow defects in MGs could be considered as those generated at the interfacial regions between two atomic clusters of VPs with geometric incompatibilities, e.g., the VPs with high ($d_5 \sim 1$) and low ($d_5 < 0.5$) local degree of five-fold symmetry, respectively.

In fact, the concept of structural defects in connection with the geometric incompatibilities in continuum solids has been well developed. It comes from a general definition of a structural defect that the geometric incompatibility in a structure could result in elastic stresses [43-44], originally used by Eshelby [43] to determine the stress field around an inclusion in continuum solids. Moshe *et al.* [45-47] formulized such definition for defects in amorphous solids. The amorphous

structures are considered as a Euclidean manifold which is translation invariant; and the defects are described by the Gaussian curvatures of their surfaces. More specifically, in a multipole expansion for the Gaussian curvature, the structural defects are then defined as those with a singularity in Gaussian curvatures. For simplicity, Moshe *et al.* [45] considered the two-dimensional (2D) localized defects in an ideal amorphous solid with isotropic structure, which could be defined by the only non-zero term, the quadrupole term, in the multipole expansion for the Gaussian curvature. Such curvature quadrupole model could quantitatively define the geometry (the 2D shape), orientation and energetics of flow defects in amorphous solids.

As discussed in Sections 3 and 4, the bond breaking analysis reveals information on the mechanistic features such as the shape, orientation and energetics of flow defects in MGs, which could be compared with those of the aforementioned curvature quadrupole model for ideal (isotropic) amorphous solid [45-47], as follows. Firstly, the shapes of flow defects revealed by the bond breaking analysis are different with that of curvature quadrupole defects. Although the aspect ratio of flow defects consisting of atoms with broken bonds can be as large as 1.8, their shape is far from being planar or two-dimensional. The reason is that in MGs the interfacial regions between two atomic clusters of VPs with geometric incompatibilities, where the flow defects are generated, could be heterogeneous and are rather rough, as shown in Fig. 8. Secondly, in terms of the orientation of flow defects, the bond breaking analysis suggests that the preference orientation of flow defects is 57° with respect to the loading direction, whereas that for the curvature quadrupole defects is 45° . Such difference could result from the structural heterogeneity in MGs, which is not accounted in the curvature quadrupole model for the ideal amorphous solid [45]. Thirdly, the energetics of curvature quadrupole defects are usually characterized by

their equilibrium separation distance R_c under an applied shear stress τ_0 [45]:

$$R_c = \left[\frac{\langle Q \rangle \mu}{8\pi B_2 \tau_0} \right]^{0.5}, \quad (6)$$

where μ is the shear modulus and $\langle Q \rangle$ is the average defect strength of quadrupole defects; B_2 is a constant. For the flow defects consisting of atoms with broken bonds, the shear stress on the flow defects can be assumed to be $\tau_0 = (\sigma - \sigma_y)/3$. As shown in Fig.9(b), their separation distance can be scaled as $\langle d_{min} \rangle = R_c \sim (\tau_0)^{-0.45}$, in consistent with that (Eq. (6)) for the curvature quadrupole defects. The good agreement between the energetics for the flow defects revealed by the bond breaking analysis and the quadrupole defects implies that the flow defects in MGs could be generated at the interfacial regions between two atomic clusters of VPs with geometric incompatibilities.

6. Conclusions

In summary, we investigate the bond breaking under uniaxial compression in a metallic glass by classical MD simulations. The bond breaking shows a close correlation with local shear strains and the behaviors of clusters of flow defects formed with the broken bonds are closely correlated with different stages of plastic deformation. The bond breaking processes are quantitatively characterized. The bonds with the same elements are much easier to be broken than those with the different elements. If the normalized projected length of a bond along the loading direction is less than about 0.4, it tends to be broken. A bond with an angle to the loading direction less than 57 degree is more difficult to break than others. Our results also show that bond breaking is closely correlated with local atomic structure such as bond pairs, local five-fold symmetry and quasi-nearest atom, suggesting that the flow defects in MGs could be generated at the interfacial regions between two local atomic clusters with geometric incompatibilities. The shape, orientation and energetics of

flow defects revealed by the bond breaking analysis are compared with those of the curvature quadrupole model for flow defects in ideal amorphous solids, which facilitate our understanding on the deformation mechanisms of MGs.

Acknowledgement

This work was supported by a grant from the Research Grants Council of the Hong Kong Special Administrative Region, China (PolyU152607/16E), the National Natural Science Foundation of China (Grant Nos. 51701135, 51571132, 51574176 and 51874209) and Major Research & Development Plan of Shanxi Province (International Cooperation project) (201603D421028).

References

- [1] G. Kumar, H.X. Tang, and J. Schroers, Nanomoulding with amorphous metals, *Nature* 457 (2009) 868-872.
- [2] A. Inoue, B. Shen, H. Koshiba, H. Kato, and A.R. Yavari, Cobalt-based bulk glassy alloy with ultrahigh strength and soft magnetic properties, *Nat. Mater.* 2 (2003) 661-663.
- [3] M.M. Trexler, and N. N. Thadhani, Mechanical properties of bulk metallic glasses, *Prog. Mater. Sci.* 55 (2010) 759-839.
- [4] J.F. Wang, R. Li, N.B. Hua, and T. Zhang, Co-based ternary bulk metallic glasses with ultrahigh strength and plasticity, *J. Mater. Res.* 26 (2011) 2072-2079.
- [5] S.J. Pang, T. Zhang, K. Asami, and A. Inoue, Synthesis of Fe–Cr–Mo–C–B–P bulk metallic glasses with high corrosion resistance, *Acta Mater.* 50 (2002) 489-497.
- [6] F.F. Wu, K.C. Chan, S.S. Jiang, S.H. Chen, and G. Wang, Bulk metallic glass composite with good tensile ductility, high strength and large elastic strain limit, *Sci. Rep.* 4 (2014) 5302.
- [7] X.K. Xi, D.Q. Zhao, M.X. Pan, W.H. Wang, Y. Wu, and J.J. Lewandowski, Fracture of brittle metallic glasses: Brittleness or plasticity, *Phys. Rev. Lett.* 94 (2005) 125510.
- [8] M. Ashby, and A. Greer, Metallic glasses as structural materials, *Scripta Mater.* 54 (2006) 321-326.
- [9] C. Schuh, T. Hufnagel, and U. Ramamurty, Mechanical behavior of amorphous

alloys, *Acta Mater.* 55 (2007) 4067-4109.

[10] J.C. Ye, J. Lu, C.T. Liu, Q. Wang, and Y. Yang, Atomistic free-volume zones and inelastic deformation of metallic glasses, *Nat. Mater.* 9 (2010) 619-623.

[11] T. Egami, T. Iwashita and W. Dmowski, Mechanical properties of metallic glasses, *Metals* 3 (2013) 77-113.

[12] Z. Lu, W. Jiao, W.H. Wang, and H.Y. Bai, Flow unit perspective on room temperature homogeneous plastic deformation in metallic glasses, *Phys. Rev. Lett.* 113 (2014) 045501

[13] F. Spaepen, A microscopic mechanism for steady state inhomogeneous flow in metallic glasses, *Acta Metall.* 25 (1977) 407-415.

[14] A.S. Argon, Plastic deformation in metallic glasses, *Acta Metall.* 27 (1979) 47-58.

[15] M.L. Falk, and J.S. Langer, Dynamics of viscoplastic deformation in amorphous solids, *Phys. Rev. E* 57 (1998) 7192-7205.

[16] Z. Wang, B.A. Sun, H.Y. Bai, and W.H. Wang, Evolution of hidden localized flow during glass-to-liquid transition in metallic glass, *Nat. Commun.* 5 (2014) 5823.

[17] Z. Wang, P. Wen, L.S. Huo, H.Y. Bai, and W. H. Wang, Signature of viscous flow units in apparent elastic regime of metallic glasses, *Appl. Phys. Lett.* 101 (2012) 121906.

[18] Y.Q. Cheng, and E. Ma, Atomic-level structure and structure–property relationship in metallic glasses, *Prog. Mater. Sci.* 56 (2011) 379-473.

[19] H.L. Peng, M.Z. Li, and W.H. Wang, Structural signature of plastic deformation in metallic glasses, *Phys. Rev. Lett.* 106 (2011) 135503.

[20] R. Zallen, *The Physics of Amorphous Solids* (John Wiley & Sons, New York, 1983).

[21] H.W. Sheng, W.K. Luo, F.M. Alamgir, J.M. Bai, and E. Ma, Atomic packing and short-to-medium-range order in metallic glasses, *Nature* 439 (2006) 419-425.

[22] W. Jiao, X.L. Wang, S. Lan, S.P. Pan, and Z.P. Lu, Propensity of bond exchange as a window into the mechanical properties of metallic glasses, *Appl. Phys. Lett.* 106 (2015) 061910.

[23] S.P. Pan, J.Y. Qin, W.M. Wang, and T.K. Gu, Origin of splitting of the second peak in the pair-distribution function for metallic glasses, *Phys. Rev. B* 84 (2011) 092201.

- [24] T. Iwashita, and T. Egami, Atomic mechanism of flow in simple liquids under shear, *Phys. Rev. Lett.* 108 (2012) 196001.
- [25] G. Wang, N. Mattern, J. Bednarcik, R. Li, B. Zhang, and J. Eckert, Correlation between elastic structural behavior and yield strength of metallic glasses, *Acta Mater.* 60 (2012) 3074-3083.
- [26] Y. Suzuki, J. Haimovich, and T. Egami, Bond-orientational anisotropy in metallic glasses observed by x-ray diffraction, *Phys. Rev. B* 35 (1987) 2162.
- [27] Y.Q. Cheng, E. Ma, and H.W. Sheng, Atomic level structure in multicomponent bulk metallic glass, *Phys. Rev. Lett.* 102 (2009) 245501
- [28] F. Shimizu, S. Ogata, and J. Li, Theory of shear banding in metallic glasses and molecular dynamics calculations, *Mater. Trans.* 48 (2007) 2923-2927.
- [29] M. Falk, and J. Langer, L. Pechenik, Thermal effects in the shear-transformation-zone theory of amorphous plasticity: comparisons to metallic glass data, *Phys. Rev. E* 70 (1998) 011507.
- [30] A. Stukowski, Visualization and analysis of atomistic simulation data with OVITO—the Open Visualization Tool, *Modelling Simul. Mater. Sci. Eng.* 18 (2010) 015012
- [31] A. Takeuchi, and A. Inoue, Classification of Bulk Metallic Glasses by Atomic Size Difference, Heat of Mixing and Period of Constituent Elements and Its Application to Characterization of the Main Alloying Element, *Mater. Trans.* 46 (2005) 2817-2829.
- [32] H.B. Yu, K. Samwer, W.H. Wang and H.Y. Bai, Chemical influence on β -relaxations and the formation of molecule-like metallic glasses, *Nat. Commun.* 4 (2013) 2204.
- [33] E.S. Park, H.J. Chang, and D.H. Kim, Effect of addition of Be on glass-forming ability, plasticity and structural change in Cu–Zr bulk metallic glasses, *Acta Mater.* 56 (2008) 3120-3131.
- [34] S.P. Pan, S.D. Feng, J.W. Qiao, B.S. Dong and J.Y. Qin, The shells of atomic structure in metallic glasses, *Modelling Simul. Mater. Sci. Eng.* 24 (2016) 025004.
- [35] Z.F. Zhang and J. Eckert, Unified tensile fracture criterion, *Phys. Rev. Lett.* 94 (2005) 094301.
- [36] J.D. Honeycutt, H.C. Andersen, Molecular dynamics study of melting and freezing of small Lennard-Jones clusters, *J. Phys. Chem.* 91 (1987) 49504963.

- [37] S.P. Pan. Study on the atomic structure of Fe-based liquid and amorphous alloys by molecular dynamics simulation:[D]. Jinan:Shandong Univ. (2012).
- [38] N.N. Medvedev, The algorithm for three-dimensional Voronoi polyhedra, *J. Comput. Phys.* 67 (1986) 223-229.
- [39] H.L. Peng, M.Z. Li, and W.H. Wang, Structural signature of plastic deformation in metallic glasses, *Phys. Rev. Lett.* 106 (2011) 135503.
- [40] S.P. Pan, S.D. Feng, J.W. Qiao, W.M. Wang, and J.Y. Qin, Correlation between local structure and dynamic heterogeneity in a metallic glass-forming liquid, *J. Alloy Compd.* 664 (2016) 65-70.
- [41] S.P. Pan, S.D. Feng, L.M. Wang, J.W. Qiao, X.F. Niu, W.M. Wang, and J.Y. Qin, Correlation between initial structure and athermal quasi-static compressive deformation in a metallic glass, *J. Alloy Compd.* 699 (2017) 274-277.
- [42] X.F. Niu, S.D. Feng, and S.P. Pan, Related Structure Characters and Stability of Structural Defects in a Metallic Glass, *Materials* 11 (2018) 468.
- [43] J.D. Eshelby, Elastic Inclusions and Inhomogeneities, in *Progress in Solid Mechanics*, I.N. Sneddon and R. Hill, eds (North-Holland, Amsterdam, 1961).
- [44] T. Mura, *Micromechanics of Defects in Solids*, 2nd ed. (Kluwer Academic Publishers, 1991)
- [45] M. Moshe, I. Levin, H. Aharoni, R. Kupferman, and E. Sharon, Geometry and mechanics of two-dimensional defects in amorphous materials, *Proc. Natl. Acad. Sci. U.S.A.* 112 (2015) 10873.
- [46] M. Moshe, E. Sharon, R. Kupferman, Elastic interactions between two-dimensional geometric defects, *Phys. Rev. E* 92 (2015) 062403.
- [47] R. Kupferman, M. Moshe, J.P. Solomon, Metric description of singular defects in isotropic materials, *Arch. Ration. Mech. Anal.* 216 (2014) 1009-1047.

Figure captions

Fig. 1 Partial PDFs for Zr–Zr, Zr–Cu and Cu–Cu pairs for the $Zr_{50}Cu_{50}$ MG at 50K. The typical atomic configuration is also displayed. The red and blue spheres represent Zr and Cu atoms, respectively

Fig. 2 The stress(σ)-strain(δ) curve under uniaxial compression at 50 K for the $Zr_{50}Cu_{50}$ MG.

Fig. 3 Distribution of local shear strain (η^{Mises}) for the atoms with different number of broken bonds and the total atoms, at an overall strain of (a) 2%, (b) 4%, (c) 6% and (d) 8%. The insets show the average local shear strain as a function of the number of broken bonds.

Fig. 4 Spatial correlation between local shear strain and the number of broken bonds **in the early stage of plastic deformation**. (a) The configuration with the atoms colored by the local shear stain at 6% overall strain. (b) The same configuration as that in (a) but with the atoms colored by the number of broken bonds.

Fig. 5 Pearson and Spearman correlation coefficients between the number of broken bonds and local shear strains as a function of the overall strains.

Fig.6 (a) The fraction of broken bonds as a function of overall strains; (b) The fraction of atoms with different broken bonds as a function of overall strains

Fig. 7 Cluster analysis of broken bonds as a function of overall strains. The clusters consist of atoms with at least one broken bond and all those atoms are initially connected by the broken bonds. (a) the number of clusters of flow defects (N_c), (b) the average size of clusters of flow defects ($\langle S_c \rangle$), (c) the size of the largest cluster (S_{max}), (d) the normalized projected lengths (NPLs) of the largest cluster of flow defects in three (x -, y - and z -) directions, **inset are the NPLs for $0 < \delta < 6\%$.**

Fig. 8 Visualization of the clusters of flow defects with a size no less than 10 atoms at (a) 2%, (b) 3%, (c) 4% and (d) 5% strains. The fact that atoms with the same color means that they belong to the same cluster of flow defects.

Fig. 9 (a) Average distance between the centre of gravity of one cluster to that of its nearest neighboring cluster $\langle d_{min} \rangle$. (b) The log-log plot of the correlation between $\langle d_{min} \rangle$ and $\sigma - \sigma_y$ (σ_y is the yield stress at 1.9% strain). The red dash line fits the data (in black circles) for $\delta = 2-4\%$.

Fig. 10 The preference of bond breaking B_{ij} with different atomic types as a function of overall strains

Fig. 11 Statistical distributions of the length of the broken bonds for (a) Zr-Zr, (b) Zr-Cu and (c) Cu-Cu, and the projected length of the broken bonds along the loading direction normalized by the maximum bond length for (d) Zr-Zr, (e) Zr-Cu and (f) Cu-Cu, at different overall strains. The short dash line shows the distributions of all the bonds before uniaxial compression.

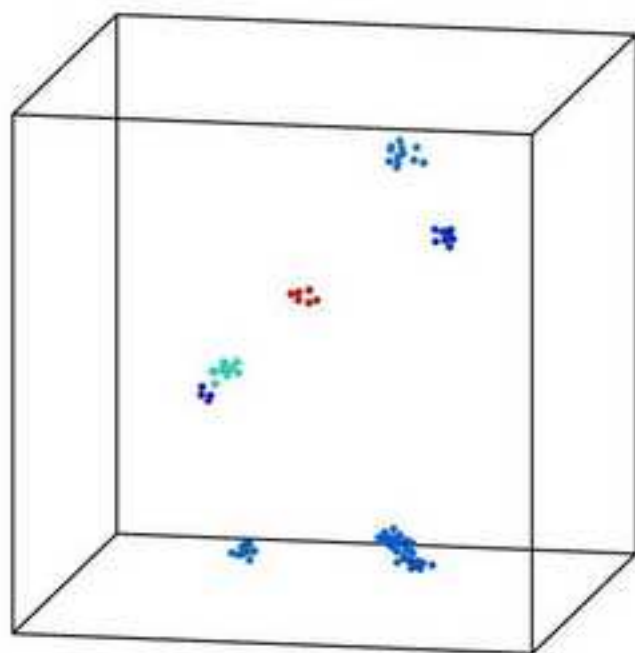
Fig. 12 Statistical distribution of the angles between the initial orientation of the broken bonds and the loading direction at different overall strains. The short dash line shows the distribution of angle between the orientation of all the bonds and the loading direction before the uniaxial compression.

Fig. 13 The statistical distribution of bond pairs before uniaxial compression. The inset is the preference of bond breaking of different bond pairs.

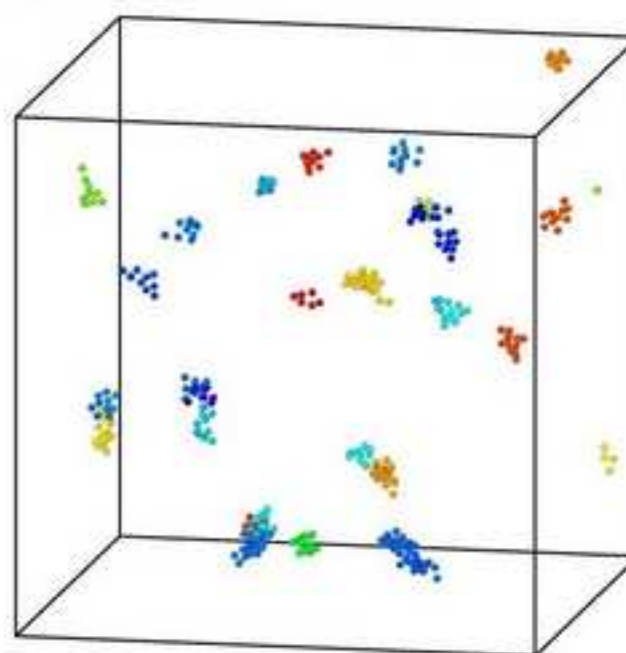
Fig. 14 (a) Histogram of the top 20 Voronoi polyhedra before uniaxial compression.

The number after the bar is the order number of five-fold symmetry of the Voronoi polyhedron, in a descending order indicated by the arrow. (b)~(e) are the color maps of the preference of bond breaking with different VP indexes, at strains of (b) 2%, (c) 4%, (d) 6%, and (e) 8%. **The order number in (b)~(e) represents the VPs with the same order number in (a).**

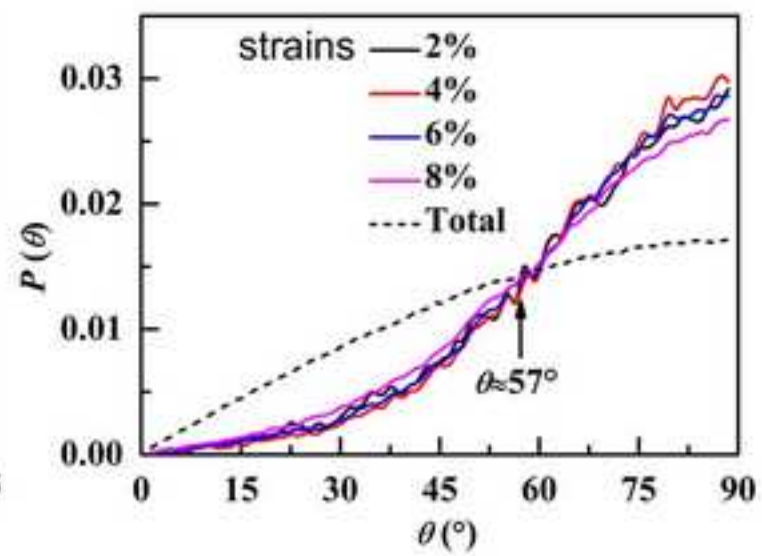
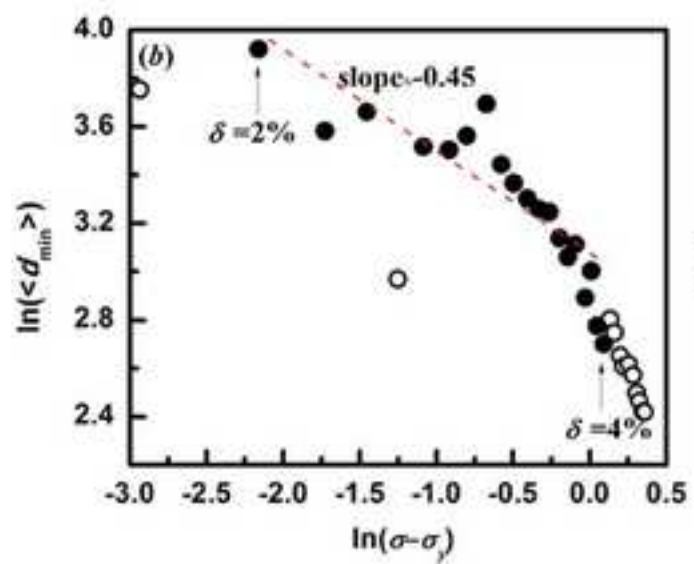
Fig.15 (a) The statistical distribution of the number of QNAs (N_Q) before uniaxial compression. (b) and (c) are the preference of bond breaking with different N_Q . i and j in i - j correspond to the value of N_Q , which belong to the pair of atoms in a bond. The term “others” refers to the atoms with N_Q no less than 4.



strain=2%



strain=3%



Highlights

Geometry, orientation and energetics of flow defects are revealed.

Chemical and structural factors are quantitatively measured.

A mechanistic model for flow defects is proposed.

Figure
[Click here to download high resolution image](#)

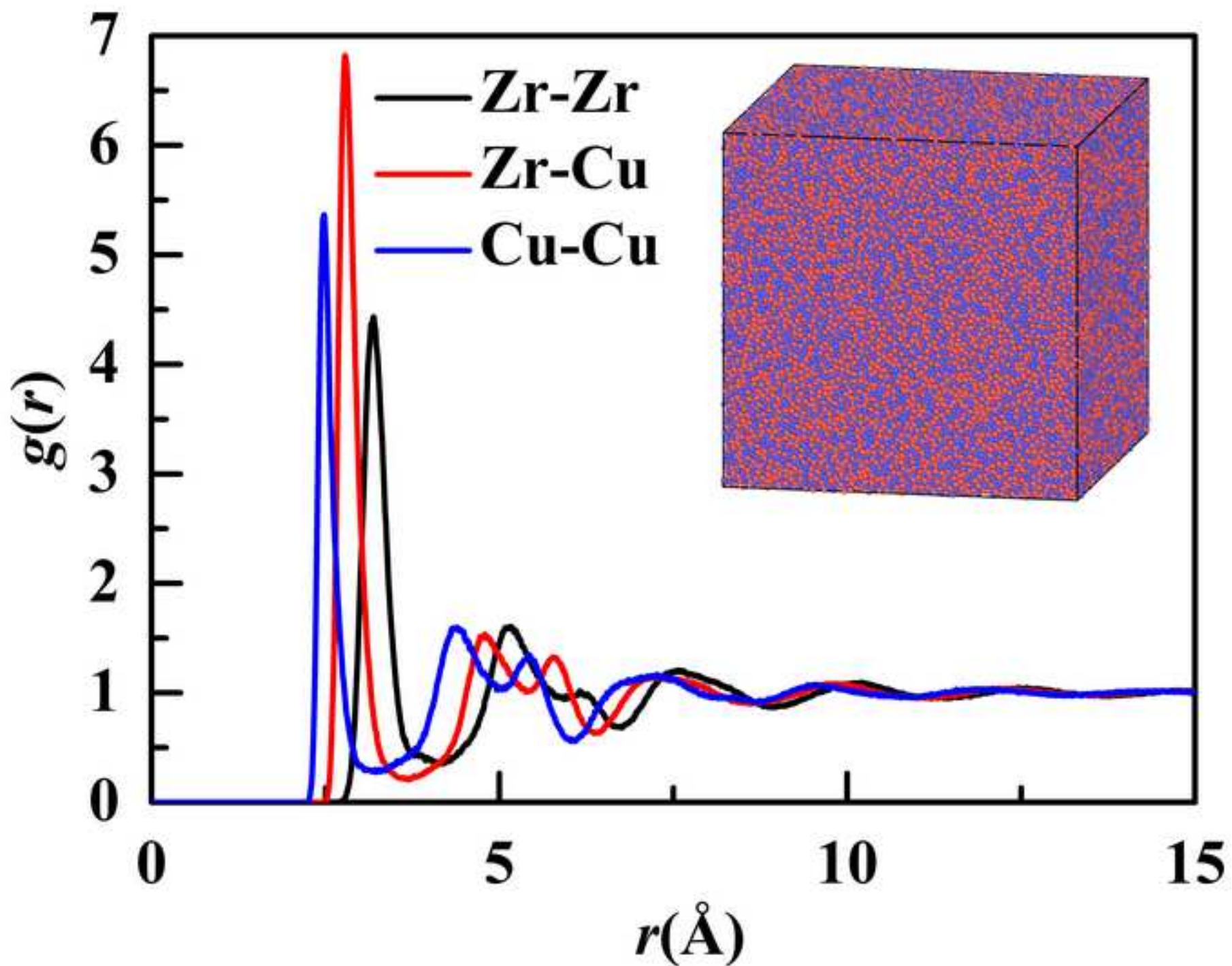


Figure
[Click here to download high resolution image](#)

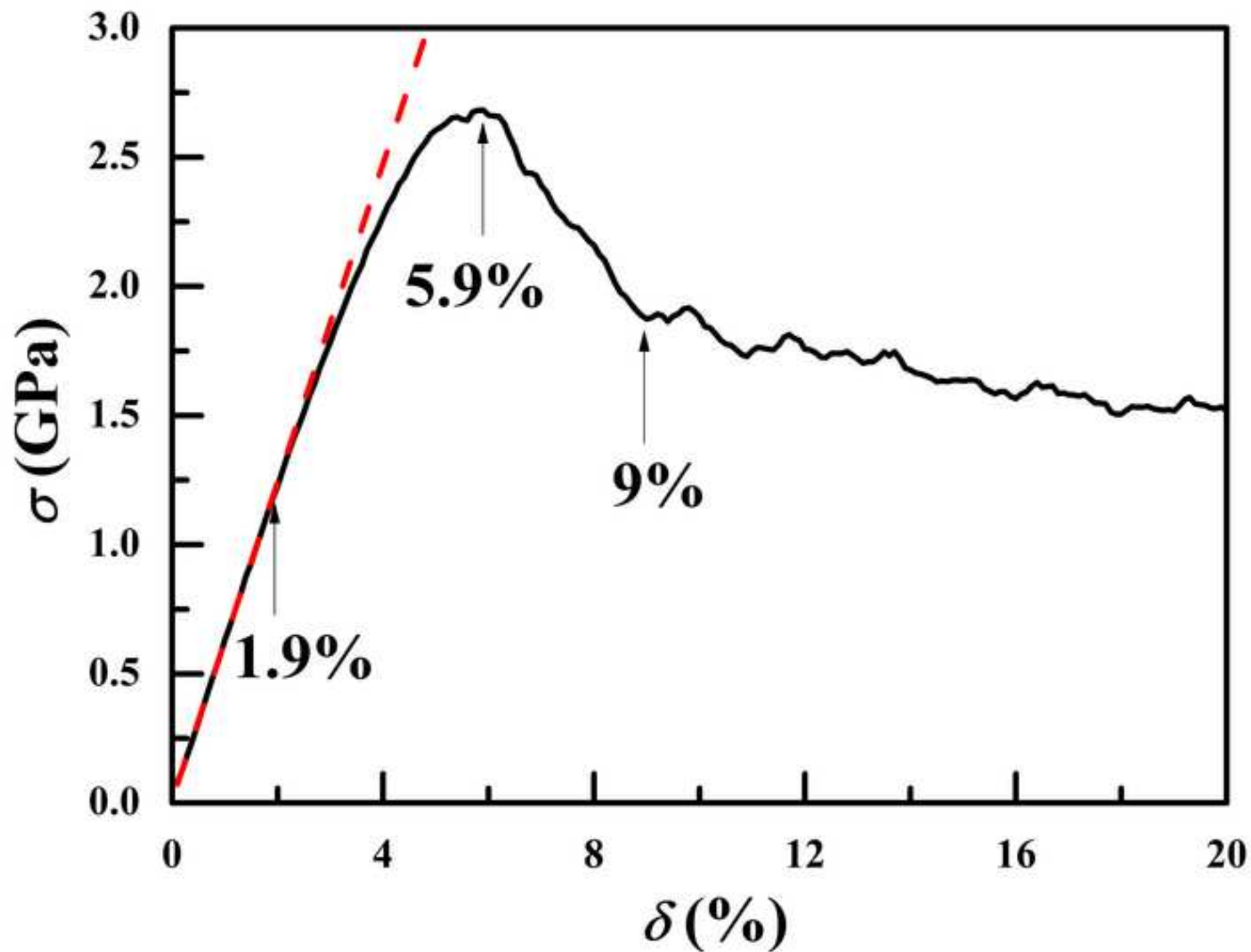
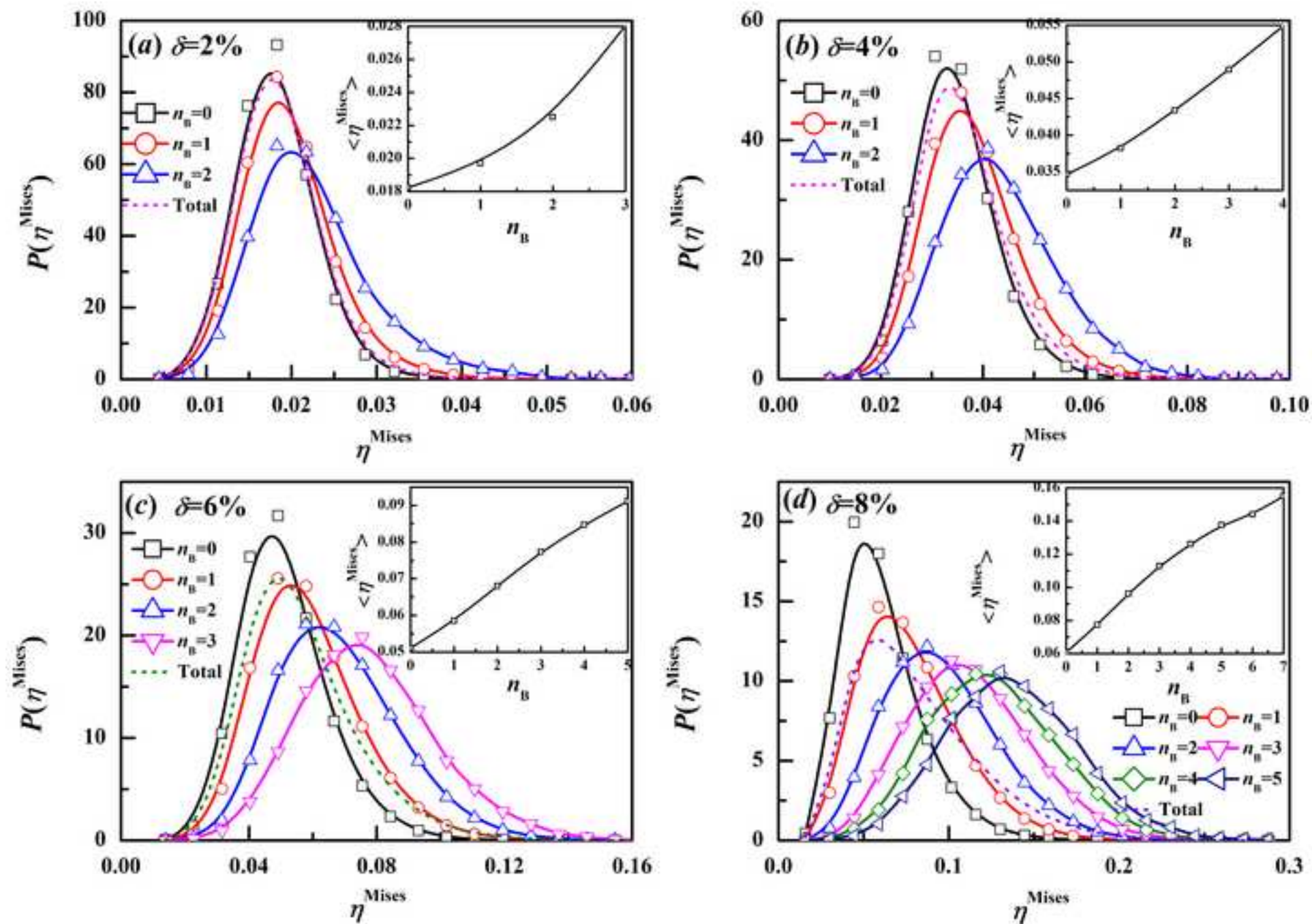


Figure
[Click here to download high resolution image](#)



Figure

[Click here to download high resolution image](#)

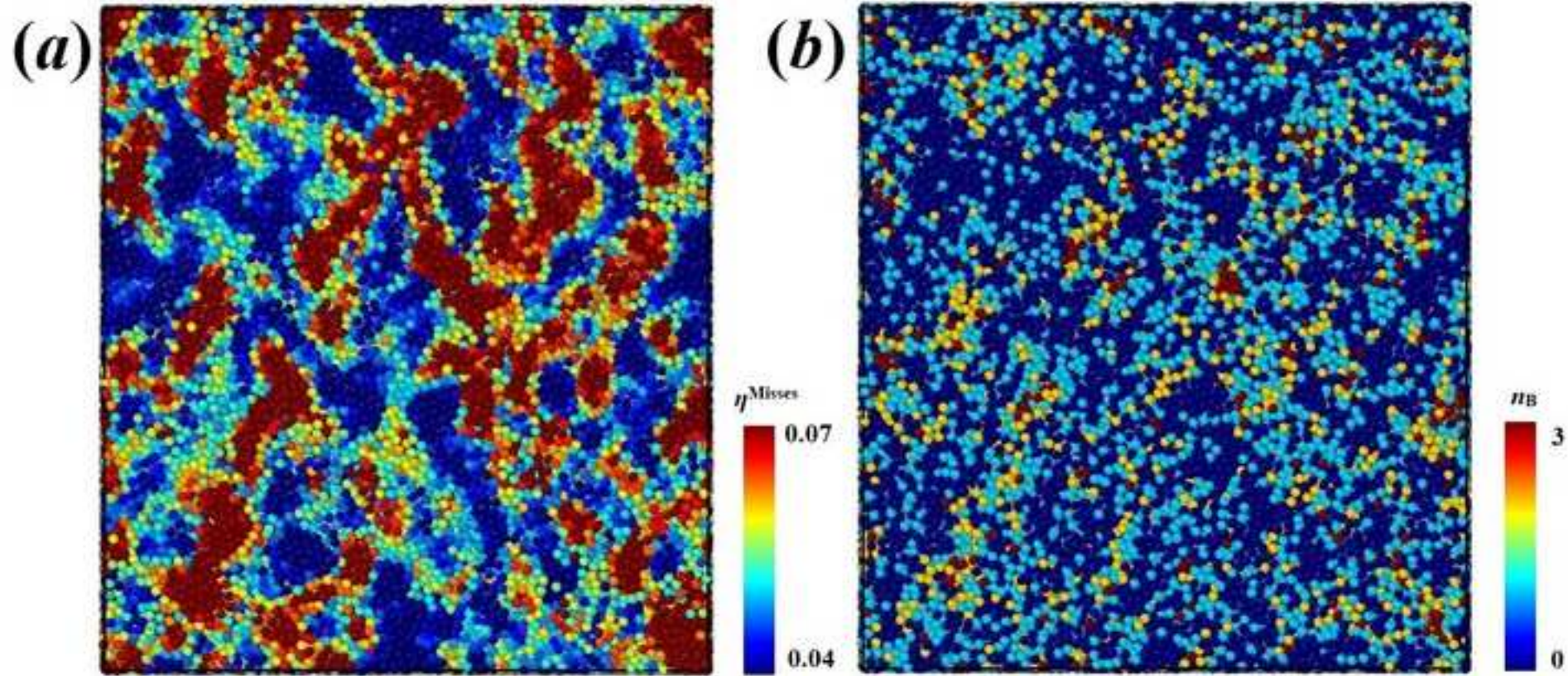
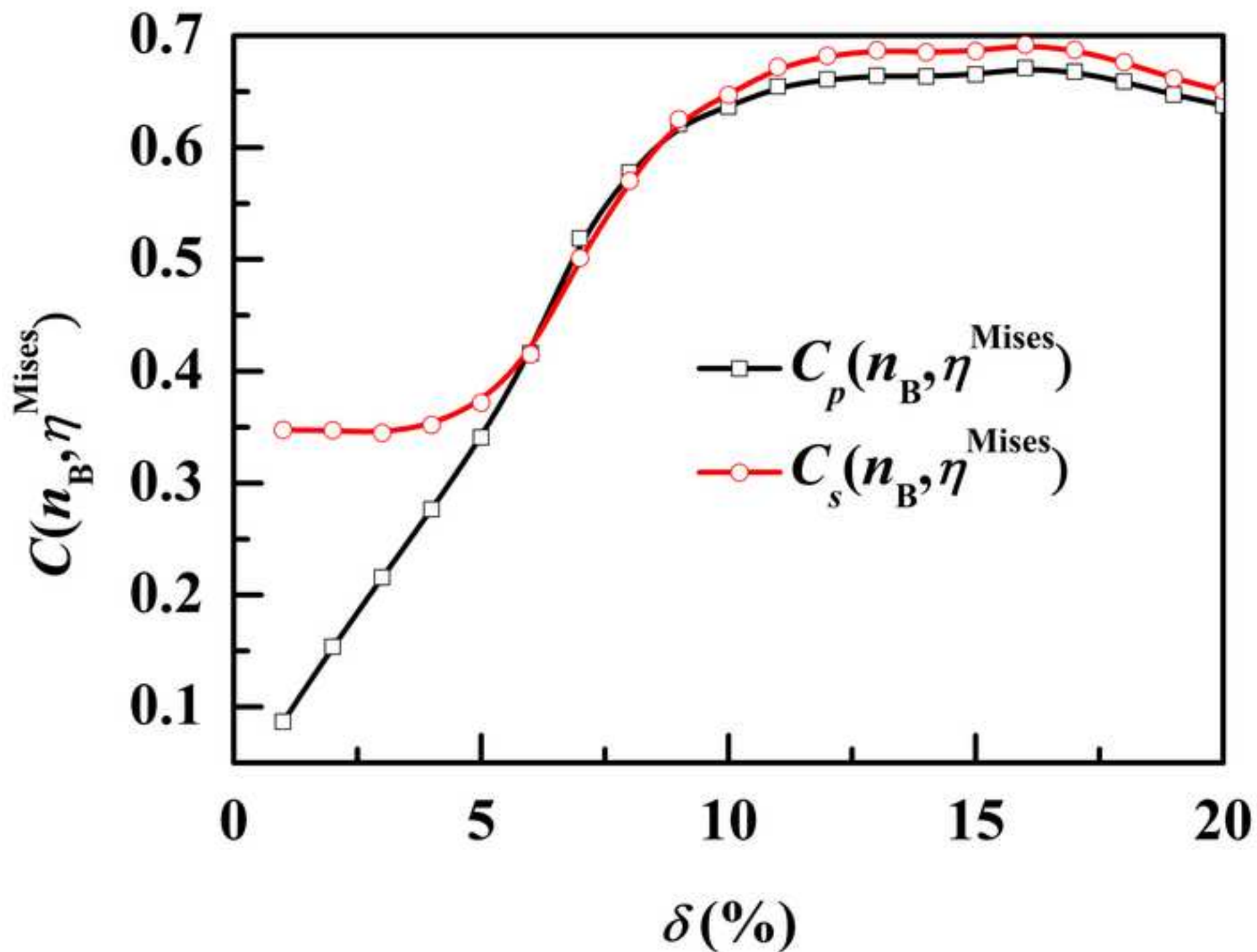


Figure
[Click here to download high resolution image](#)



Figure

[Click here to download high resolution image](#)

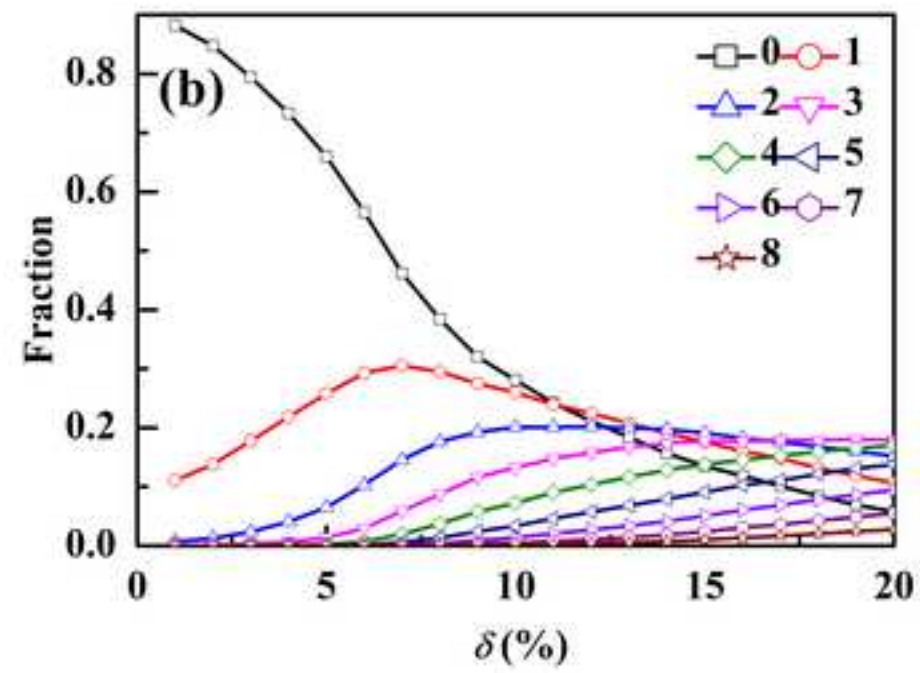
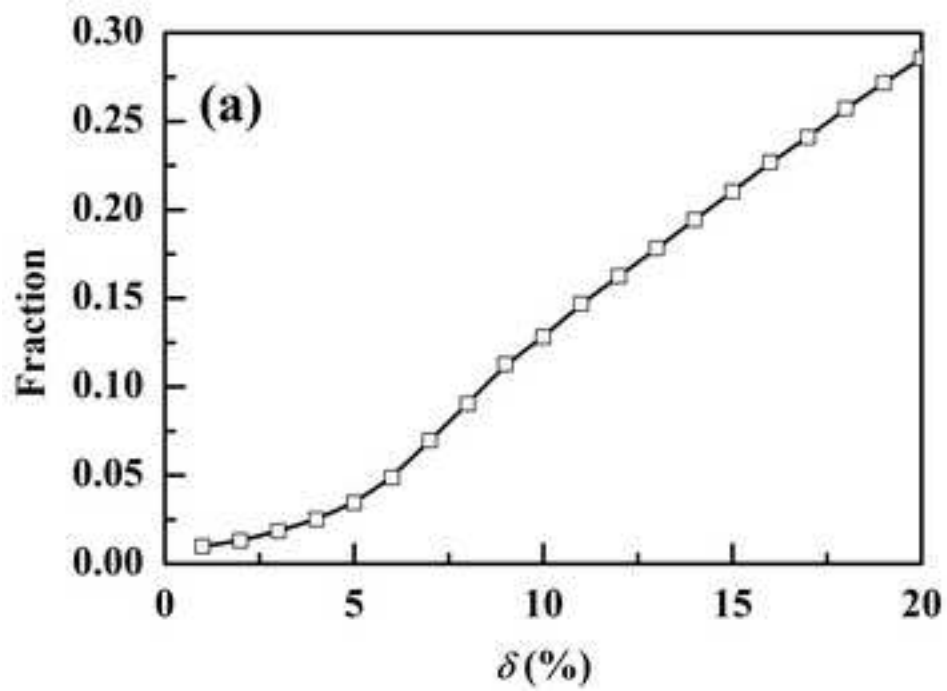
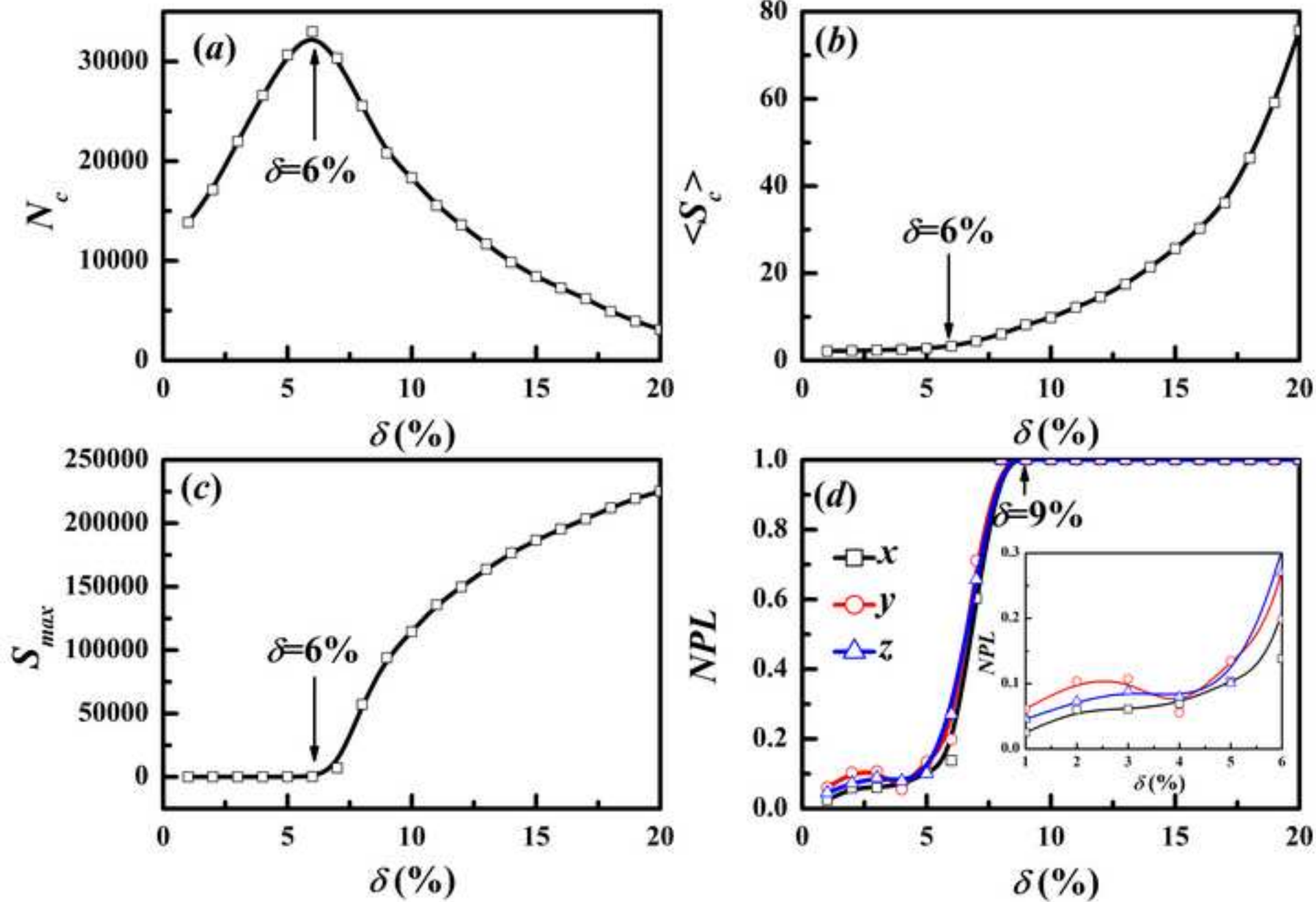
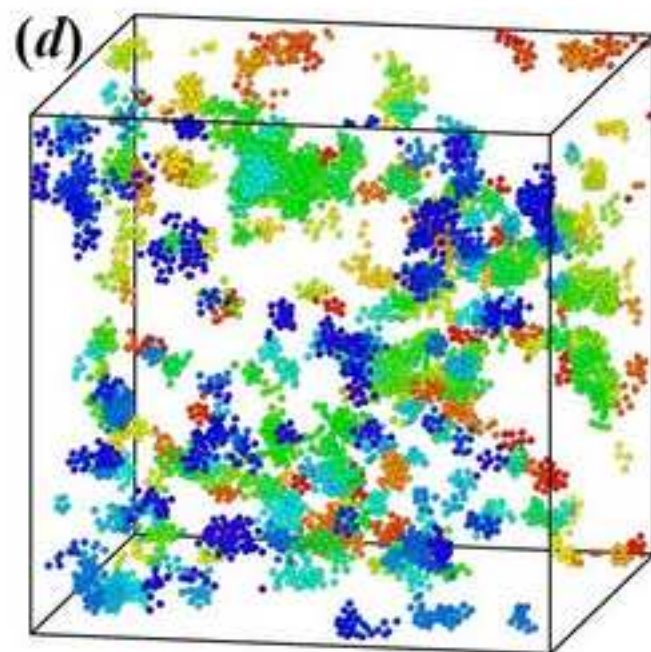
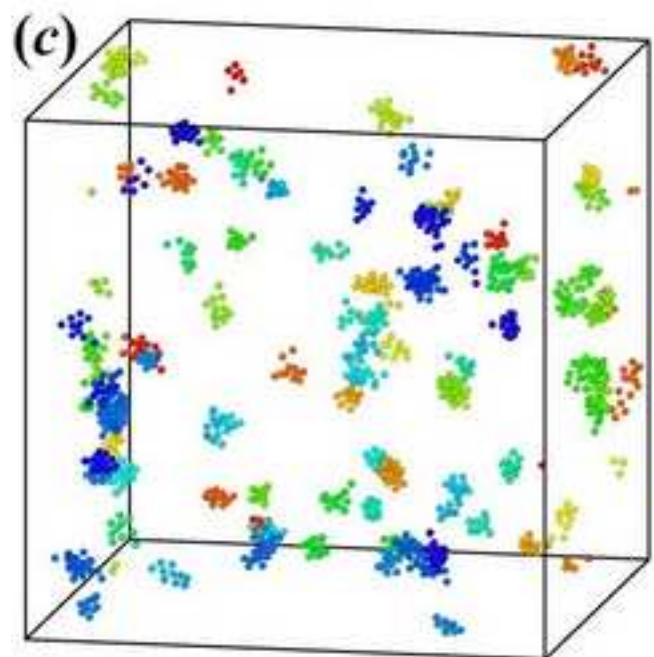
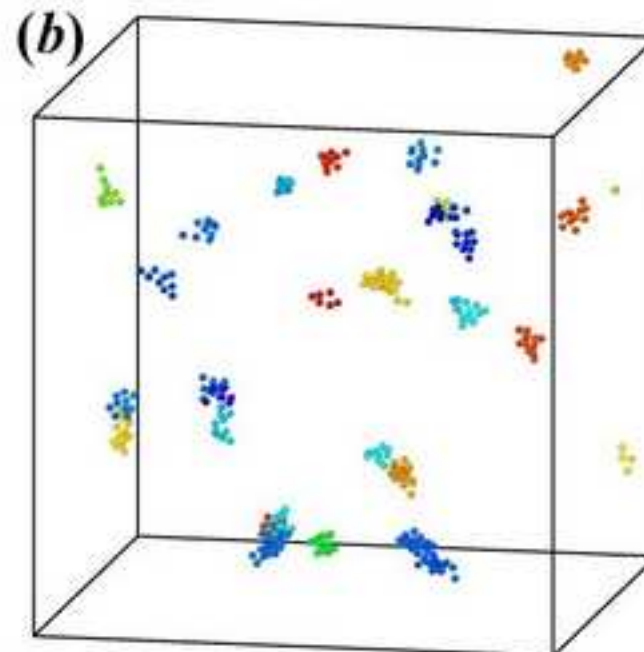
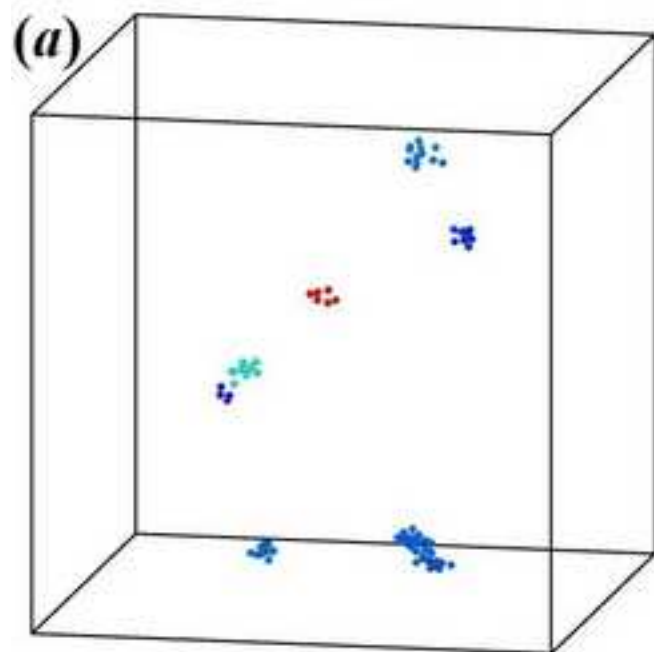


Figure
[Click here to download high resolution image](#)



Figure

[Click here to download high resolution image](#)



Figure

[Click here to download high resolution image](#)

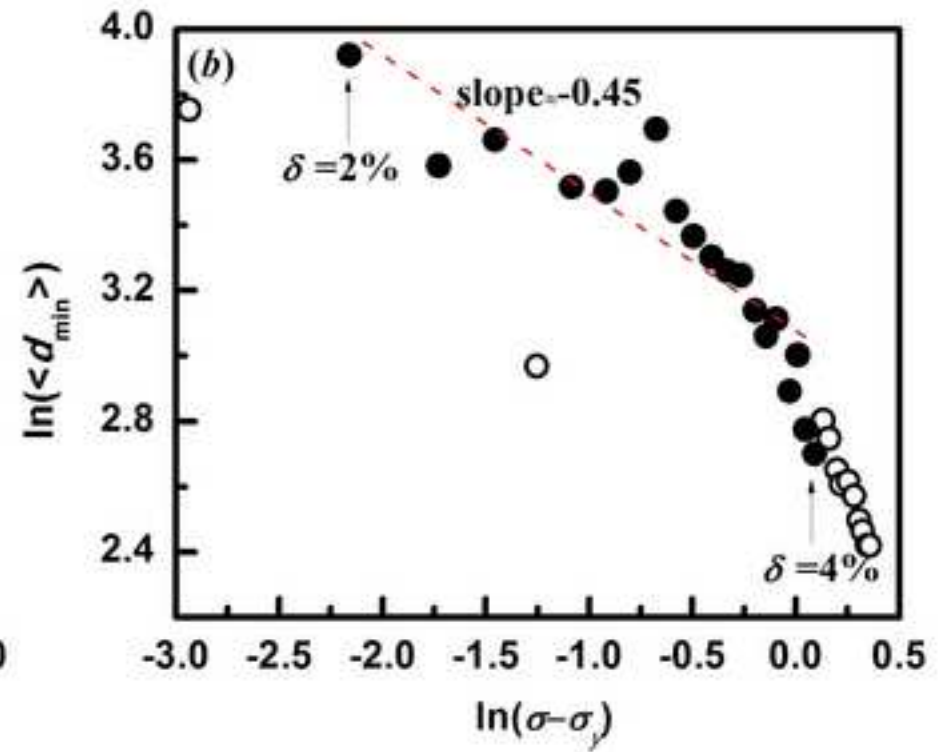
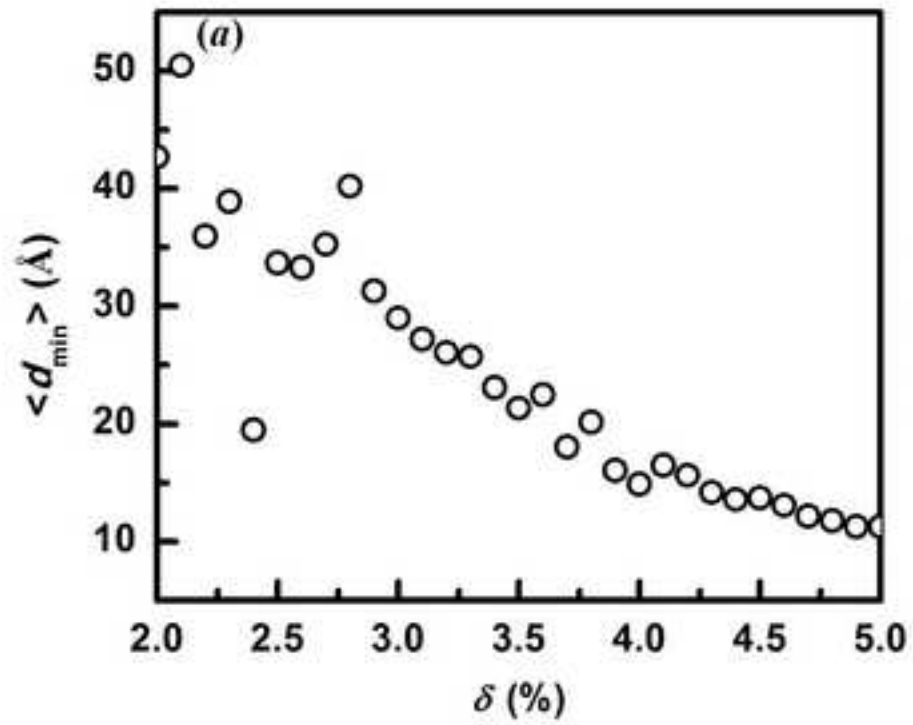
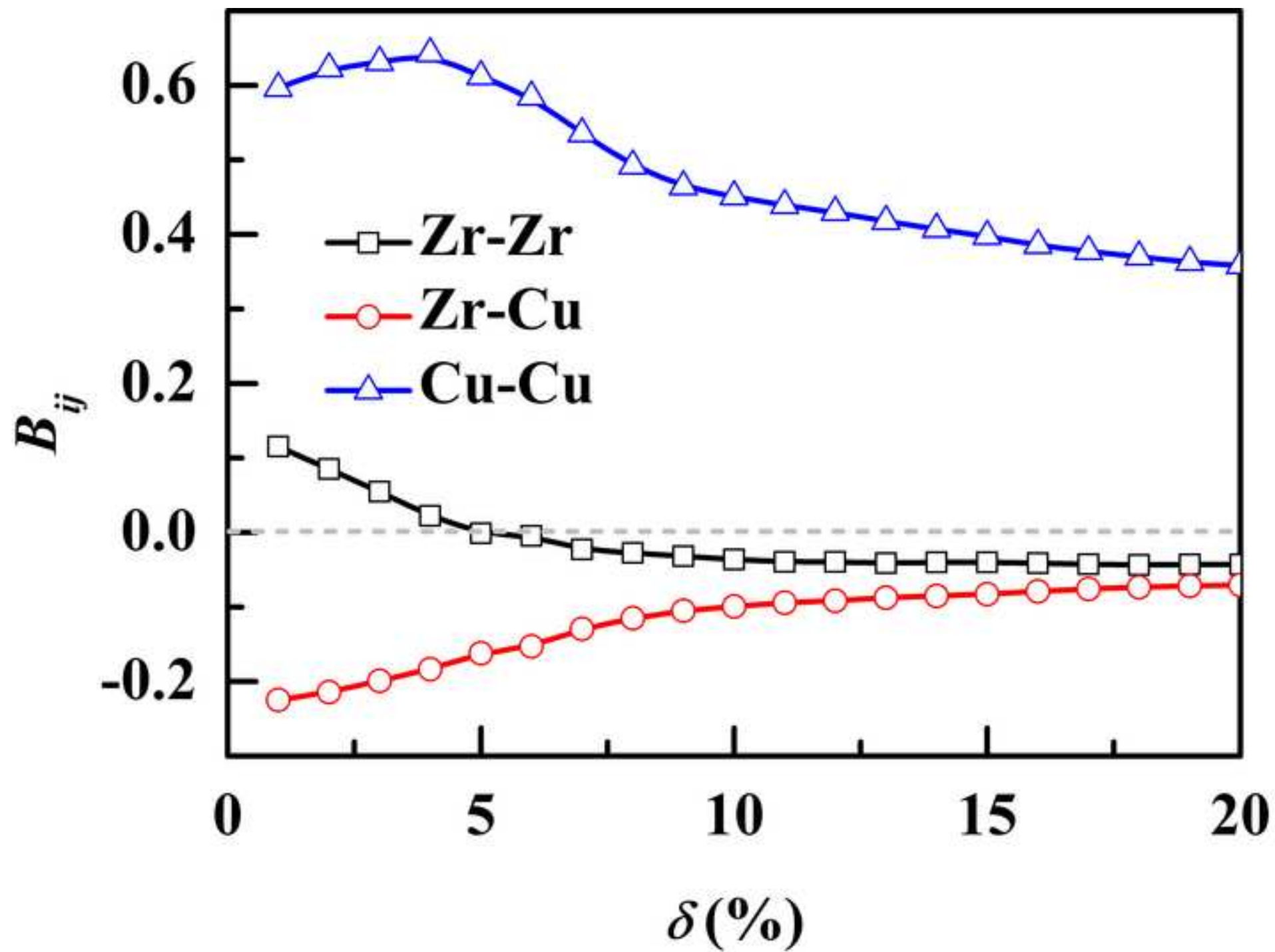


Figure
[Click here to download high resolution image](#)



Figure

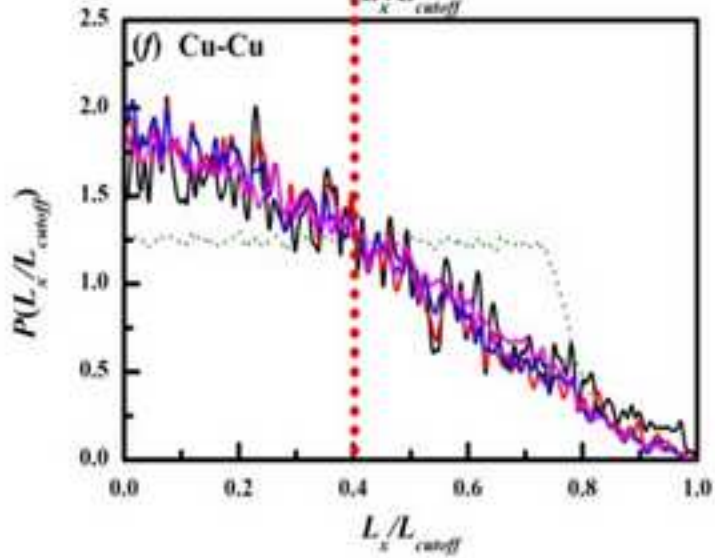
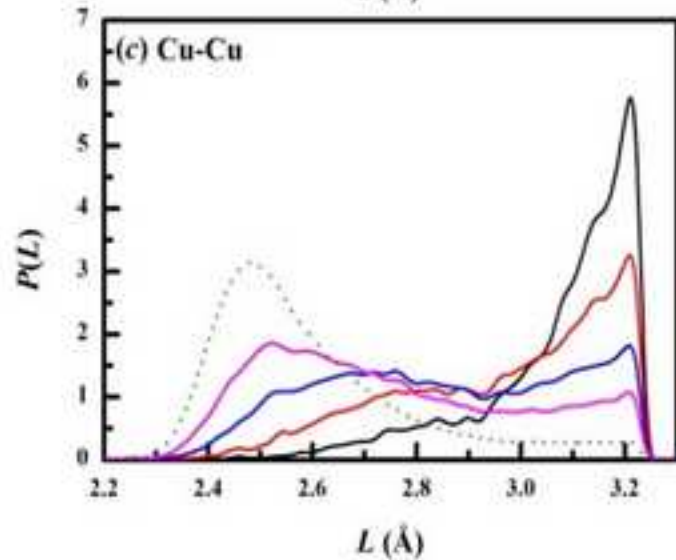
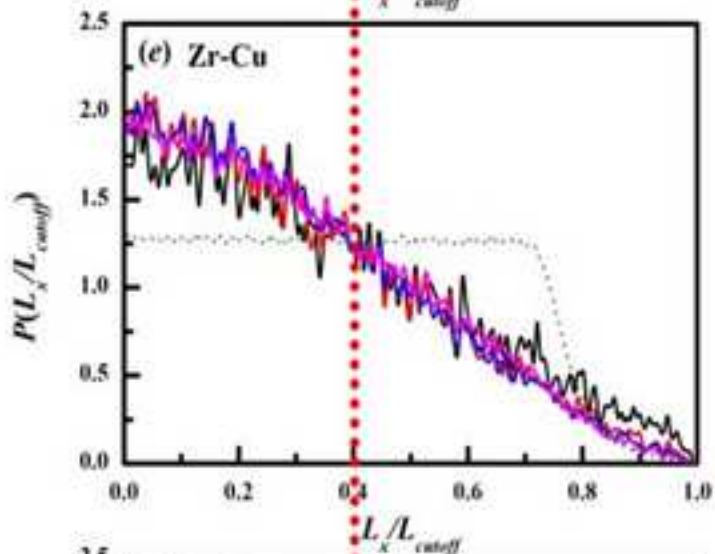
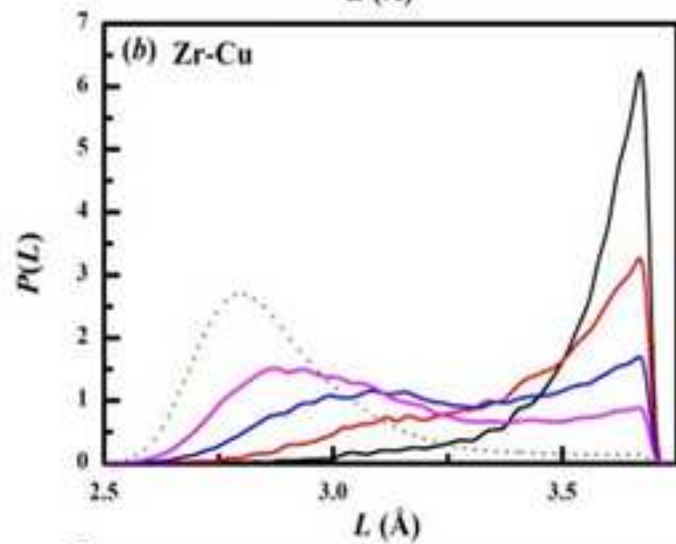
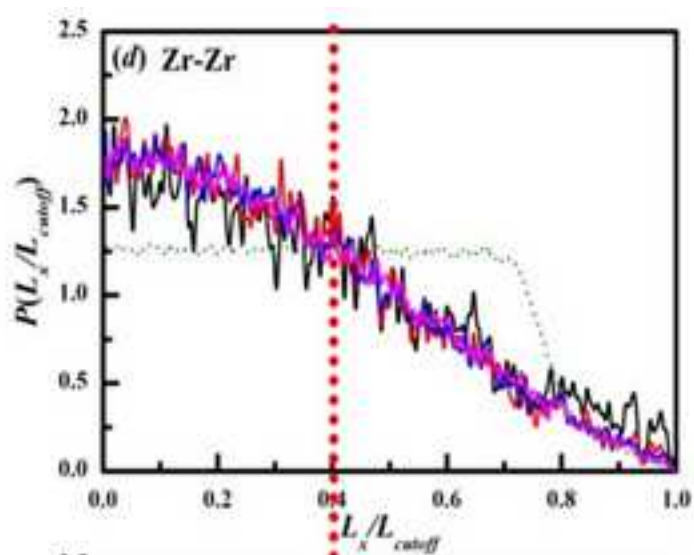
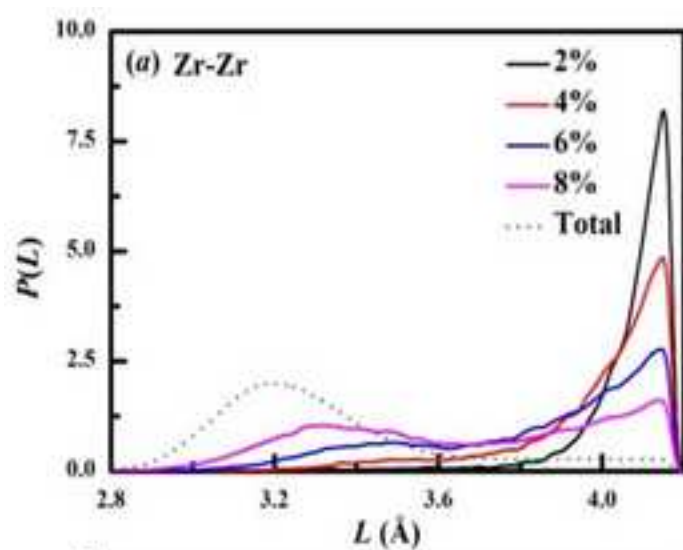
[Click here to download high resolution image](#)

Figure
[Click here to download high resolution image](#)

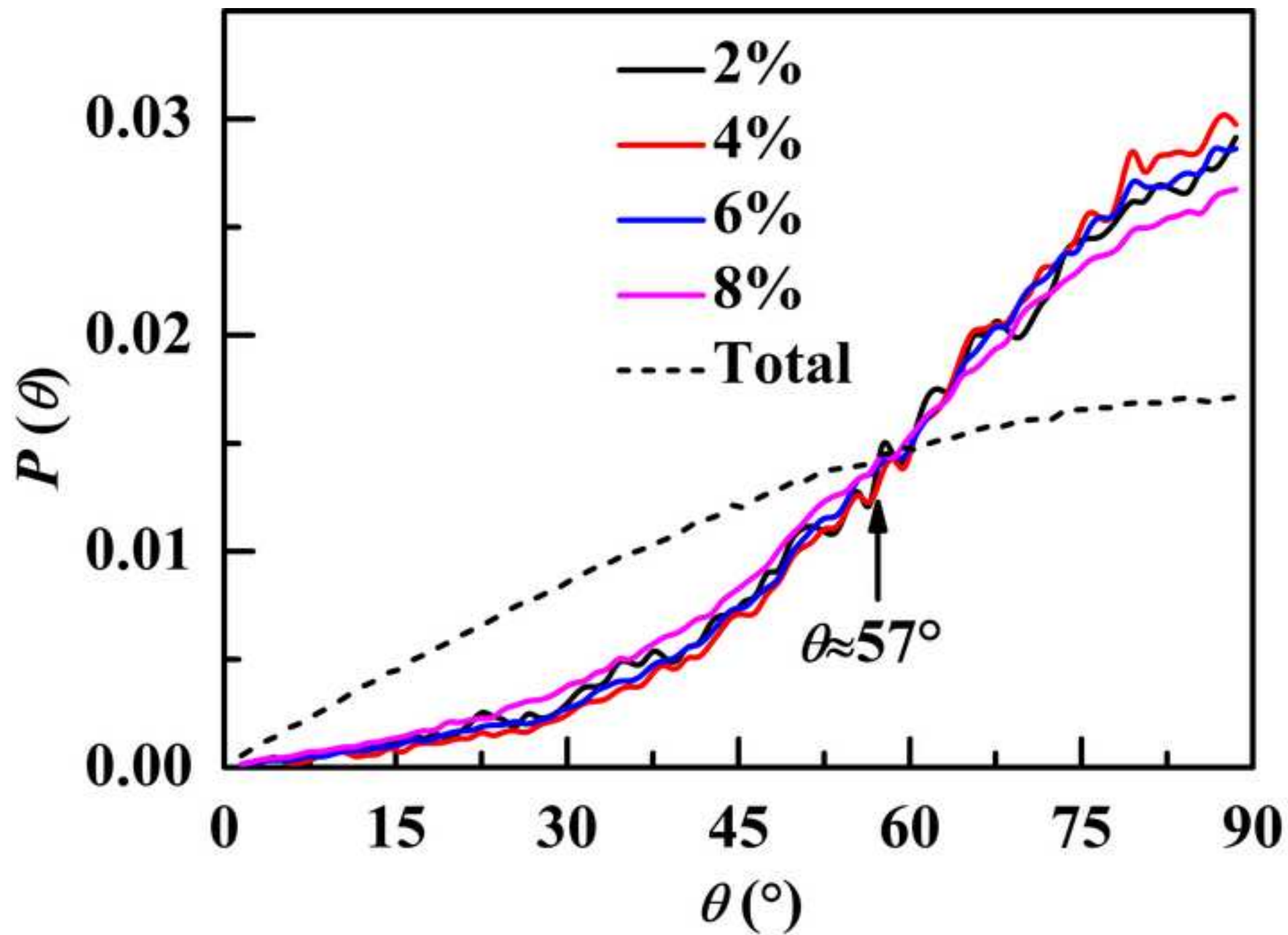


Figure
[Click here to download high resolution image](#)

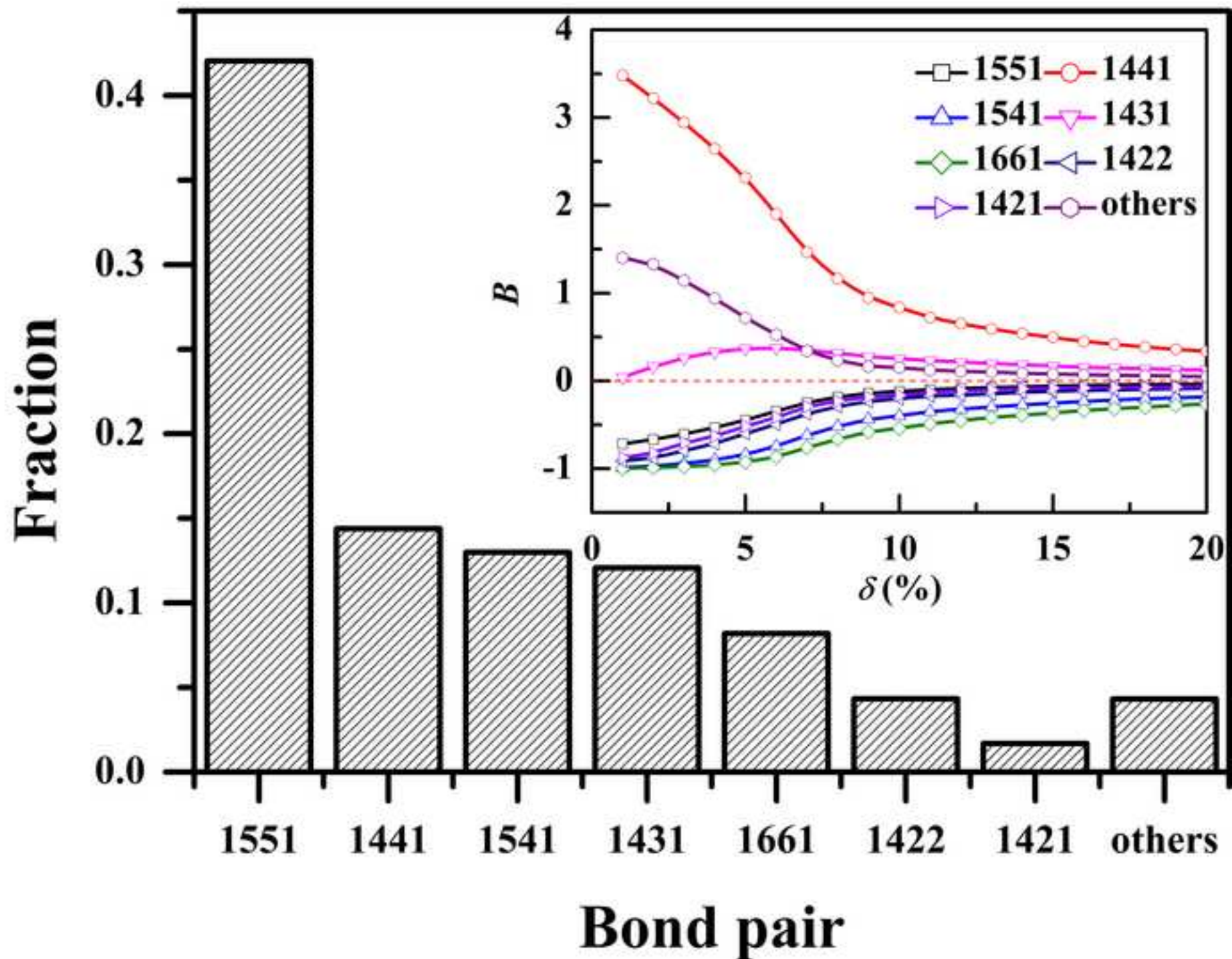
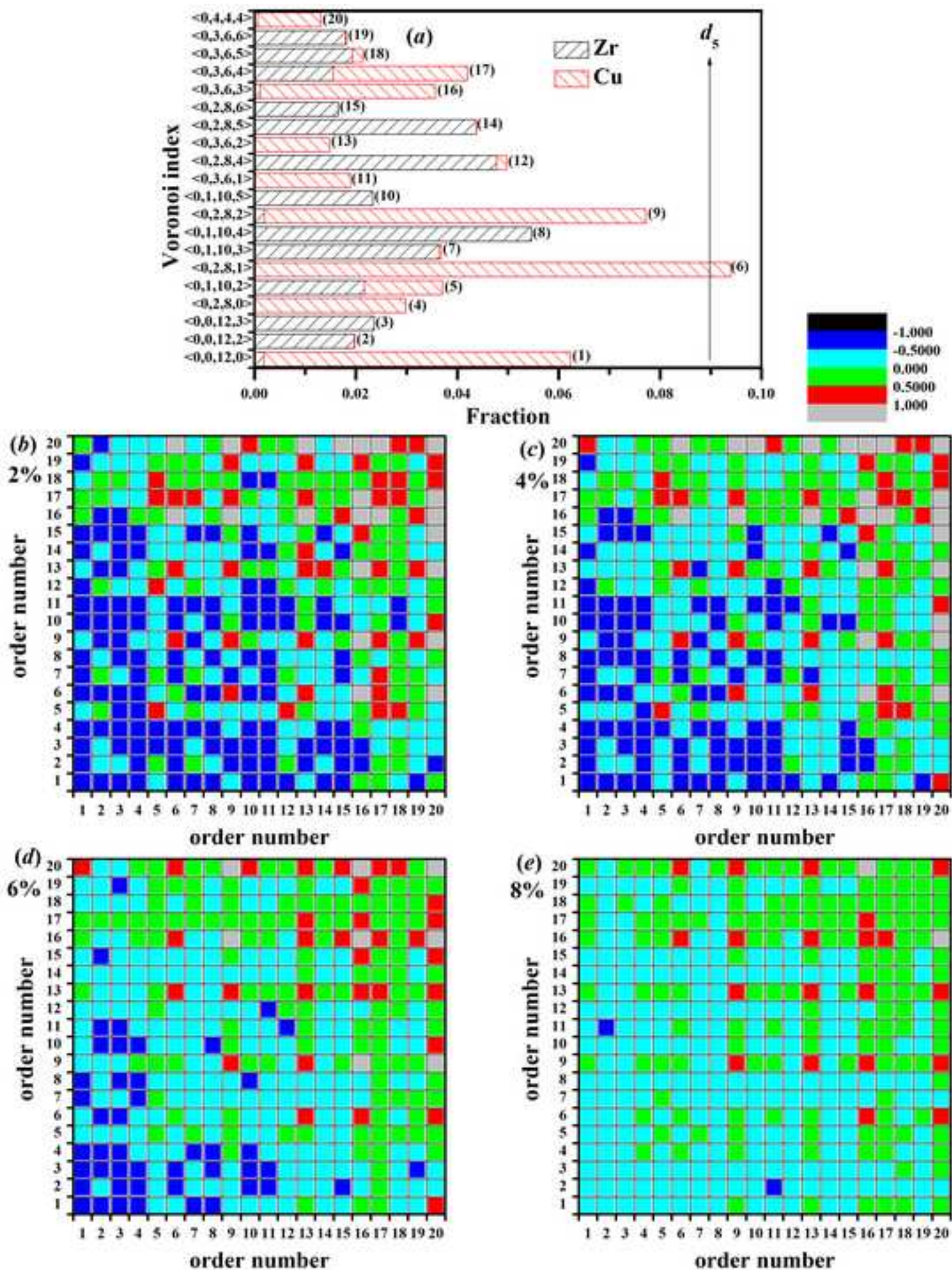


Figure
[Click here to download high resolution image](#)



Figure

[Click here to download high resolution image](#)